Lack of Correlations between Cold Molecular Gas and AGN Properties in Type 1 AGNs at z □ 0.5

The Astrophysical Journal, 950:60 (15pp), 2023 June 10 https://doi.org/10.3847/1538-4357/acc9b4

Lack of Correlations between Cold Molecular Gas and AGN Properties in Type 1 AGNs at $z \lesssim 0.5$

Juan Molina[1,2], Jinyi Shangguan[3], Ran Wang[1,4], Luis C. Ho[1,4], Franz E. Bauer[5,6,7], and Ezequiel Treister[5,6]
[1] Kavli Institute for Astronomy and Astrophysics, Peking University, Beijing 100871, People's Republic of China; jumolina@pku.edu.cn
[2] Department of Space, Earth and Environment, Chalmers University of Technology, Onsala Space Observatory, SE-439 92 Onsala, Sweden
[3] Max-Planck-Institut für Extraterrestrische Physik (MPE), Giessenbachstr., D-85748 Garching, Germany
[4] Department of Astronomy, School of Physics, Peking University, Beijing 100871, People's Republic of China
[5] Instituto de Astrofísica, Facultad de Física, Pontificia Universidad Católica de Chile, Campus San Joaquín, Av. Vicuña Mackenna 4860, Macul Santiago 7820436, Chile
[6] Centro de Astroingeniería, Facultad de Física, Pontificia Universidad Católica de Chile, Campus San Joaquín, Av. Vicuña Mackenna 4860, Macul Santiago 7820436, Chile
[7] Millennium Institute of Astrophysics, Nuncio Monseñor Sótero Sanz 100, Of 104, Providencia, Santiago, Chile
Received 2023 January 8; revised 2023 March 16; accepted 2023 March 31; published 2023 June 9

Abstract

We present new NOrthern Extended Millimeter Array (NOEMA) observations of the CO(2–1) emission in eight of the brightest Palomar-Green quasars at $z \lesssim 0.5$ to investigate the role of active galactic nucleus (AGN) feedback in luminous quasars detected at low redshifts. We detect CO(2–1) emission in three objects, from which we derive CO luminosities, molecular gas masses and fractions, and gas depletion times. In combination with data available in the literature, we build a total sample of 138 local type 1 AGNs with CO(2–1) measurements. We compare the AGN properties with the host galaxy molecular gas properties, considering systems nondetected in CO emission. We find that the CO luminosity does not correlate with AGN luminosity and Eddington ratio, while the molecular gas fraction is weakly correlated with Eddington ratio. The type 1 AGNs can be roughly separated into two populations in terms of infrared-to-CO luminosity ratio, with one population presenting values typically found in normal star-forming systems, while the other having lower ratio values, comparable to those measured for starbursts. We find no evidence that AGN feedback rapidly quenches star formation in type 1 AGNs. Our results may imply an underlying the role of host galaxy gravitational instabilities or the fast inflow of cold gas in triggering AGN activity.

Unified Astronomy Thesaurus concepts: AGN host galaxies (2017); Quasars (1319); Submillimeter astronomy (1647)

1. Introduction

The evolution of galaxies is tightly correlated with the growth of their supermassive black holes (BHs) as evidenced by the correlations between the BH mass and the host galaxy bulge properties (Magorrian et al. 1998; Ferrarese & Merritt 2000; Gebhardt et al. 2000). The connection between BH accretion and host galaxy growth naturally arises because both depend on the same fuel reservoir, replenished largely by similar processes that drive gas inward (Kormendy & Kennicutt 2004). The coevolution of the BH and host galaxy (Kormendy & Ho 2013) is widely accepted to be regulated by feedback from an active galactic nucleus (AGN; Fabian 2012). During the accretion of mass onto the BH, vast amounts of energy are released, and a merely minor fraction of this power coupled to the BH surroundings can heat and/or expel gas from the host galaxy (e.g., Somerville et al. 2008; Schaye et al. 2015; Sijacki et al. 2015; Nelson et al. 2018), thereby halting the ongoing star formation activity (Dubois et al. 2016). AGN feedback can also affect the galaxy halo, preventing the condensation of cold and warm gas, and further hamper star formation over long timescales (Bower et al. 2006; Croton et al. 2006; Fabian 2012; Gaspari et al. 2020).

During the last decade, numerous efforts have been focused on testing whether AGN feedback effectively removes sufficient cold gas from the host galaxy to curtail ongoing star formation activity. Studies focusing on comparisons with control samples and/or the main sequence of star-forming galaxies have reported no difference between inactive galaxies and those hosting AGNs (Rosario et al. 2018; Kirkpatrick et al. 2019; Schulze et al. 2019; Florez et al. 2020; Koss et al. 2021; Salvestrini et al. 2022; Smirnova-Pinchukova et al. 2022; but see Vito et al. 2014; Scholtz et al. 2018; Stemo et al. 2020). Correlations between key host galaxy properties, such as molecular hydrogen (H_2) content, star formation rate (SFR), and/or star formation efficiency, with AGN luminosity suggest that low-z luminous AGNs are mainly hosted in typical star-forming galaxies (e.g., Harrison et al. 2012; Rosario et al. 2012, 2013; Zhang et al. 2016; Stanley et al. 2017; Husemann et al. 2017; Bernhard et al. 2019; Grimmett et al. 2020; Jarvis et al. 2020; Yesuf & Ho 2020; Koss et al. 2021; Vietri et al. 2022), while the more-luminous active systems tend to be found in starbursts (e.g., Young et al. 2014; Bernhard et al. 2016; Pitchford et al. 2016; Kirkpatrick et al. 2020; Shangguan et al. 2020a; Xie et al. 2021; Zhuang et al. 2021). Only a few studies of high-z AGNs ($z \approx 1-2$) suggest reduced molecular gas content in AGN hosts (Kakkad et al. 2017; Perna et al. 2018; Bischetti et al. 2021; Circosta et al. 2021). Whether or how a luminous AGN does efficiently remove or heat the gas from host galaxy and affect the ongoing star formation is still uncertain (Harrison et al. 2017).

Optically visible and largely unobscured quasars—the most-luminous AGNs—allows us to study the possible effects of AGN feedback on their host galaxies. An unobscured quasar is

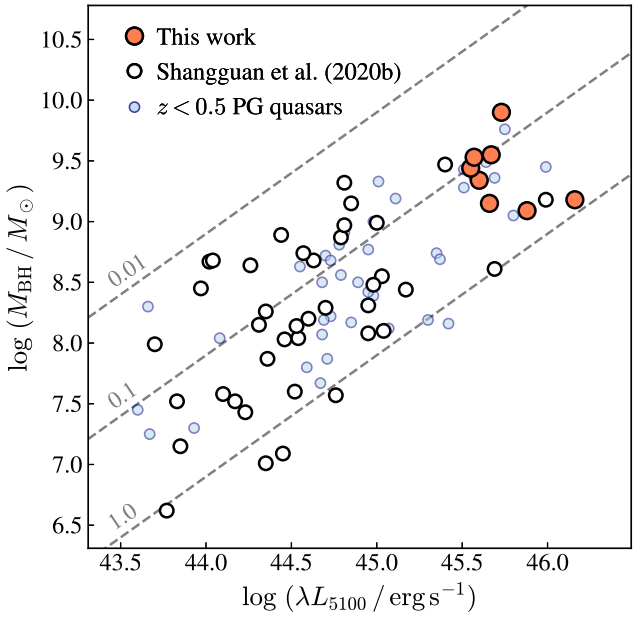

Figure 1. BH mass as a function of the AGN monochromatic luminosity at 5100 Å for PG quasar host galaxies. The red-filled circles present the eight targets observed by NOEMA and analyzed in this work. The open circles show PG quasars with previous CO observations (Shangguan et al. 2020b), while the blue circles correspond to the parent sample of $z \lesssim 0.5$ PG quasars observed by Herschel (Shangguan et al. 2018). The dashed lines represent constant Eddington ratio values. We target a subsample of PG quasars with more massive BHs and luminous AGNs, complementing the previous CO observations.

thought to arise after the overwhelming release of energy from the AGN that expels the gas and dust enshrouding the nucleus (e.g., Sanders et al. 1988; Hopkins et al. 2008). Strikingly, the study of the global IR (∼1–500 μm) spectral energy distribution (SED) emission in a set of 87 local ($z < 0.5$) Palomar-Green (PG) quasars (Boroson & Green 1992) suggested that most of these unobscured AGNs have dust-based molecular gas masses comparable to normal star-forming galaxies with similar stellar mass (Shangguan et al. 2018). Follow-up Atacama compact array (ACA) observations targeting carbon-monoxide molecule (^{12}CO) emission and previous literature observations confirmed the results from the global IR SED analysis. CO $J = 2 \rightarrow 1$ transition [$\nu_{\rm rest} = 230.538$ GHz; hereafter CO(2–1)] emission was detected in a total 34 out of 40 PG quasars. The global CO emission-line shapes further suggested that the molecular gas appears kinematically regular within the host galaxies (Shangguan et al. 2020a, 2020b; see also Molina et al. 2021). However, the PG quasar sample observed in CO is admittedly biased toward less-luminous local PG quasars ($L_{\rm bol} \lesssim 10^{45}$ erg s^{-1}; Figure 1). Luminous AGNs can drive multiphase outflows and deposit their energy into the host galaxy interstellar medium (ISM; Cicone et al. 2014; Feruglio et al. 2015; Perna et al. 2015; Morganti 2017; Cicone et al. 2018; Fluetsch et al. 2019; Veilleux et al. 2020; Girdhar et al. 2022). The outflow energetics correlate with AGN luminosity (molecular gas mass outflow rates $\propto L_{\rm bol}^{0.76}$ and kinetic power $\propto L_{\rm bol}^{2.27}$; Fiore et al. 2017) meaning that the AGN feedback effect on the host galaxy ISM, if any, should be more easily detected in more-luminous AGNs.

In this work, we report new NOrthern Extended Millimeter Array (NOEMA) observations targeting CO(2–1) for a subsample of eight $z \approx 0.3-0.5$ PG quasars selected from Shangguan et al. (2018). Those targets correspond to the more-luminous PG quasars at $z \lesssim 0.5$. By using complementary data taken from the literature, we build a total sample of 138 unobscured local AGNs covering the $L_{\rm bol} \approx 10^{43}$–$10^{47}$ erg s^{-1} range to study the relation between host galaxy molecular gas content and AGN activity, and to explore whether AGN feedback is effectively operating in those sources. The paper is organized as follows. Section 2 presents our sample, observation strategy, and data reduction. The data analysis is described in Section 3, and the subsequent results are described in Section 4. We further discuss our findings in Section 5. Section 6 presents the conclusions. We adopt a Λ-cold dark matter (ΛCDM) cosmology with $\Omega_m = 0.308$, $\Omega_\Lambda = 0.692$, and $H_0 = 67.8$ km s^{-1} Mpc^{-1} (Planck Collaboration et al. 2016).

2. Sample and Observations

We focus on observing eight PG quasars taken from the broader sample of 87 $z < 0.5$ quasars belonging to the PG survey (Boroson & Green 1992). The PG quasars were selected by their optical/ultraviolet colors, and correspond to luminous, broad-lined (type 1) AGNs. Multiwavelength data are available across the entire electromagnetic spectrum range, from the X-ray (Reeves & Turner 2000; Bianchi et al. 2009) through the optical (Boroson & Green 1992; Ho & Kim 2009), mid-IR (Shi et al. 2014; Xie et al. 2021; Xie & Ho 2022), far-IR (Petric et al. 2015; Shangguan et al. 2018; Zhuang et al. 2018), millimeter (Shangguan et al. 2020a, 2020b), and radio (Kellermann et al. 1989, 1994; Silpa et al. 2020) wavelengths, allowing detailed SED characterization and accurate estimation of the global SFR and gas content of the host galaxies (Shangguan et al. 2018). A major fraction of the sample has been already observed in the optical and near-IR by the Hubble Space Telescope (HST) at ∼0.″1 resolution (Kim et al. 2008; Zhang et al. 2016; Kim & Ho 2019; Zhao et al. 2021), while arcsecond resolution interferometric and integral field unit data are accessible for a few of these (Molina et al. 2021, 2022).

Shangguan et al. (2020a) presented CO(2–1) observations for a representative sample of 40 $z < 0.3$ PG quasars, 23 newly observed host galaxies using ACA (synthesized beam FWHM ∼ 6″). They reported line emission detection in 34 host galaxies, 21 sources detected from their ACA campaign. For the ACA data, Shangguan et al. (2020a) computed the global CO velocity integrated fluxes by spatially collapsing the spectra over the 2σ contour region of the imaged data, to then fit the emission line using a single Gaussian or double-horn profile function.

We selected the eight PG quasar host galaxies to complement and expand the sample already observed in CO(2–1) emission, specially at high AGN luminosities ($\lambda L_{5100} \gtrsim 10^{45.5}$ erg s^{-1}) where Shangguan et al. (2020a) only reported CO(2–1) measurements for three host galaxies (Figure 1). Our selection was based on requiring (1) PG quasars with AGN monochromatic luminosities at 5100 Å (λL_{5100}) higher than $10^{45.5}$ erg s^{-1} and (2) targets with robust AGN/host galaxy far-IR SED decomposition performed by Shangguan et al. (2018). The first criterion implies that we build a combined sample of PG quasars spanning ∼2 orders of magnitude in terms of λL_{5100} and BH mass (Figure 1). The second criterion ensures that the host galaxies have accurate estimates for dust 8–1000 μm far-IR luminosity, so that their SFRs could be reliably computed. We show the properties of our targets in Table 1.

The CO(2–1) emission line was observed with NOEMA on 2022 April 6–18, as part of the program W21CI (PI: J. Molina).

Table 1
Basic Parameters of the Sample

Object	R.A. (J2000.0)	Decl. (J2000.0)	z	Morphology	$\log M_{\star}$ ($M_{\odot}$)	$\log \lambda L_{5100}$ (erg s^{-1})	$\log M_{\rm BH}$ ($M_{\odot}$)	$L_{\rm bol}/L_{\rm Edd}$
(1)	(2)	(3)	(4)	(5)	(6)	(7)	(8)	(9)
PG 1049−005	10:51:51.45	−00:51:17.7	0.357	Merger	11.1*	45.60	9.34	0.14
PG 1100+772	11:04:13.86	+76:58:58.2	0.313	Elliptical	11.27	45.55	9.44	0.10
PG 1259+593	13:01:12.96	+59:02:06.7	0.472	Elliptical	10.99	45.88	9.09	0.49
PG 1425+267	14:19:03.82	+26:32:14.5	0.366	Elliptical	11.15	45.73	9.90	0.05
PG 1512+370	15:14:43.07	+36:50:50.3	0.371	Elliptical	11.01	45.57	9.53	0.09
PG 1704+608	17:04:41.37	+60:44:30.5	0.371	Elliptical	11.52	45.67	9.55	0.10
PG 2112+059	21:14:52.58	+06:07:42.4	0.466	Elliptical	10.8*	46.16	9.18	0.76
PG 2251+113	22:54:10.42	+11:36:38.7	0.323	Elliptical	11.05	45.66	9.15	0.26

Note. (1) Source name. (2) Right ascension. (3) Declination (4) Redshift. (5) Morphology of the host galaxy (Zhang et al. 2016; Zhao et al. 2021) (6) Stellar mass; the 1σ uncertainty is 0.3 dex (Shangguan et al. 2018). (7) AGN monochromatic luminosity at 5100 Å. We assume a 1σ error of 0.05 dex (Vestergaard & Peterson 2006). (8) BH mass, estimated by applying the calibration of Ho & Kim (2015) and taken from Shangguan et al. (2018); the 1σ uncertainty is 0.3 dex. (9) Eddington ratio, where $L_{\rm bol} = 10\,L_{5100}$ (Richards et al. 2006) is the bolometric luminosity, and $L_{\rm Edd} = 1.26 \times 10^{38}(M_{\rm BH}/M_{\odot})$ erg s^{-1} is the Eddington luminosity. (*) The stellar mass values are taken from Zhao et al. (2021), but carry large uncertainties (∼0.7–0.9 dex).

The observations were carried out using 10 or 11 antennas in compact array (D) configuration, dual polarization, and for total sample observing time of 22 hr. We used the autocorrelator PolyFix, which covers a total bandwidth of 15.5 GHz in each linear polarization, and split between the lower sideband (LSB) and the upper sideband (USB). The channel width is 2 MHz, namely 3.4 km s^{-1} at the tuning frequency (set in the USB) of our observations. The synthesized beam FWHM size is 1.″0–3.″7, corresponding to scales between 5 and 21 kpc at the redshifts of our sources. The observational setup for each source is detailed in Table 2.

2.1. Data Reduction

We reduced the data following the standard procedure using the GILDAS software (Guilloteau & Lucas 2000). The data were calibrated using the Institute for Radio Astronomy in the Millimeter Range (IRAM) package Continuum and Line Interferometer Calibration (CLIC). The standard pipeline reduction and calibration was implemented to a large extent, but some minor fraction of data scans was flagged following the astronomer's on duty report.[8] We imaged the data using the MAPPING software of GILDAS. We used the `uv_cont` task to combine all the line-free channels in both sidebands (we also avoided the noisy channels), and then we merged those using `uv_merge` to produce the continuum *uv* table for each source. To produce the emission-line *uv* table we subtracted the continuum using `uv_base` from the calibrated *uv* tables in the USB. Then, we used the task `uv_compress` to set the data spectral resolution. For PG 1049−005 and PG 1259+593 we set the channel width to ∼40 km s^{-1} as both were detected in CO emission at a high signal-to-noise ratio (S/N). For the rest of the sample we set a channel width ∼100 km s^{-1} after exploring different spectral setup aiming to maximize CO line detection.[9] For both, the continuum and the emission-line *uv* tables, we produced dirty images using the task `uvmap` and estimated the data rms level (Table 3). Those values broadly correspond to our observation sensitivity requirements. The image pixel size is set to 0.″2 following `uvmap` task recommendation. We used the `CLEAN` algorithm in the version of Högbom (1974) to do data deconvolution. We use natural weighting to maximize the observation sensitivity. We set `CLEAN` down to the data rms level by doing as many iterations as needed. After doing the cleaning, we visually checked the residual maps, finding no emission higher than the noise level in any target. The data are corrected for primary beam. Finally, the imaged data were converted to the usual `FITS` format using the task `vector/fits`. We consider a conservative systematic NOEMA flux calibration uncertainty of 20% at 2 mm (see footnote 8).

2.2. IR SED

To estimate the IR luminosity decontaminated from AGN effects for our targets, we benefit from the panchromatic IR SED from ∼1 to 500 μm, complemented by mid-IR (5–38 μm) spectra from the Spitzer Infrared Spectrometer (IRS), and available radio data collated in Shangguan et al. (2018). Briefly, in the near-IR the fluxes were rederived by Shangguan et al. (2018) from Two Micron All Sky Survey (2MASS; Skrutskie et al. 2006) *J*-, *H*-, and K_s- band (Cohen et al. 2003) images using a 7″ aperture radius with the sky annulus set to a radius of 25″–35″. Shangguan et al. (2018) also reestimated the mid-IR Wide-field Infrared Survey Explorer (WISE; Wright et al. 2010; Jarrett et al. 2011) *W*1 (3.353 μm) and *W*2 (4.603 μm) fluxes for the PG quasars, but avoided including the *W*3 (11.561 μm) and *W*4 (22.088 μm) data due to known systematic uncertainties associated to the red colors of the targets, plus the bands' wavelengths overlap with the bandpass of the Spitzer IRS spectra. The WISE *W*1 and *W*2 fluxes were computed using a similar method to that used for the 2MASS images. An aperture radius of 8.″25, plus a sky annulus of 50″–70″ were adopted. Coadded point-spread functions (PSFs) for the WISE bands were used to compute the aperture correction factors. Herschel Photodetector Array Camera and Spectrometer (PACS; Poglitsch et al. 2010) and Spectral and Photometric Imaging Receiver (SPIRE; Griffin et al. 2010) observations were formally presented in Shangguan et al. (2018) for the PG quasars. For the PACS data, point-source aperture photometry was performed using a 12″, 12″, and 22″ aperture radius for the 70, 100, and 160 μm bands,

[8] https://www.iram.fr/IRAMFR/GILDAS/doc/pdf/pdbi-cookbook.pdf

[9] The target PG 2251+113 was found offset by 2.″2 and −2.″7 in R.A. and decl., respectively, from the expected location. We corrected the observation pointing by this offset using `uv_shift` before proceeding with the continuum and emission-line *uv* tables construction.

Table 2
NOEMA Observational Setup

Object (1)	Observation Date (2)	Bandpass and Flux Calibrator (3)	Amplitude and Phase Calibrator (4)	PWV (mm) (5)	Observing Time* (hr) (6)	Beam Size ($'' \times ''$) (7)	Beam Position Angle (°) (8)	Half-power Beamwidth ($''$) (9)	Maximum Recoverable Scale** ($''$) (10)
PG 1049−005	10 Apr 2022	3C84	1044+018/J1028−0236	3	1.5	3.3×1.0	11	29.7	9.9
PG 1100+772	6/14 Apr 2022	3C345	1039+811/1044+719	4	4.1	2.8×1.1	40	28.7	12.1
PG 1259+593	13 Apr 2022	3C279	1300+580/J1259+516	5–6	2.6	2.4×1.5	127	32.2	12.8
PG 1425+267	6 Apr 2022	3C273	1417+273/J1422+323	4	1.1	2.4×1.3	110	29.9	14.5
PG 1512+370	10 Apr 2022	3C279	3C345/1504+377/1505+428	2	2.6	2.4×1.0	71	30.0	11.3
PG 1704+608	14/15 Apr 2022	0851+202/2013+370	1637+574/1645+635	3–6	2.2	3.0×1.3	98	30.0	11.7
PG 2112+059	6 Apr 2022	3C345	2059+034/2121+053	4	1.5	3.5×1.4	18	32.0	13.8
PG 2251+113	17/18 Apr 2022	2013+270/2230+114	3C454.3/2230+114	1–3	6.4	3.7×1.4	12	29. 5	14.5

Note. (*) Including overheads.

Table 3
Flux Density and Derived Properties of the Sample

Object	$S_{\rm cont}$	$\sigma_{\rm cont}$	$S_{\rm CO}\Delta v$	$\nu_{\rm obs}$	FWHM	$\sigma_{\rm CO}$	$\log L_{\rm IR}$	$\log L'_{\rm CO(2-1)}$	$\log M_{\rm H_2}$
	(mJy)	(mJy beam^{-1})	(Jy km s^{-1})	GHz	km s^{-1}	(mJy)	(erg s^{-1})	(K km s^{-1} pc^2)	$M_\odot$
(1)	(2)	(3)	(4)	(5)	(6)	(7)	(8)	(9)	(10)
PG 1049−005	0.52 ± 0.11	0.04	2.53 ± 0.51	170.300	181 ± 5	0.52	45.4	9.64 ± 0.09	10.13
PG 1100+772	22.37 ± 4.47	0.24	$\lesssim$2.09	⋯	⋯	2.00	44.8	⋯	⋯
PG 1259+593	$\lesssim$1.78	0.03	0.73 ± 0.16	157.403	111 ± 10	0.75	44.7	9.35 ± 0.10	9.85
PG 1425+267	4.69 ± 0.94	0.06	$\lesssim$0.59	⋯	⋯	0.54	44.9	⋯	⋯
PG 1512+370	5.75 ± 1.15	0.04	$\lesssim$0.39	⋯	⋯	0.36	44.6	⋯	⋯
PG 1704+608	3.34 ± 0.67	0.07	$\lesssim$0.83	⋯	⋯	0.77	45.1	⋯	⋯
PG 2112+059	$\lesssim$2.40	0.05	0.75 ± 0.33	157.093	398 ± 169	0.68	45.2	9.35 ± 0.17	9.85
PG 2251+113	8.98 ± 1.80	0.13	$\lesssim$0.52	⋯	⋯	0.49	44.6	⋯	⋯

Note. (1) Source name. (2) Millimeter continuum flux density at rest-frame 230 GHz. (3) Noise level of the continuum image. (4) CO(2–1) velocity integrated intensity. (5) CO(2–1) emission line observed frequency. (6) FWHM. (7) Noise level of the cleaned data cube. (8) Total IR luminosity of the host galaxy calculated following Shangguan et al. (2018). The typical uncertainty is ∼0.2–0.3 dex. (9) CO(2–1) line luminosity. (10) Molecular gas mass derived from the CO luminosity, assuming $\alpha_{\rm CO} = 3.1\ M_\odot\ ({\rm K\ km\ s^{-1}\ pc^2})^{-1}$. The 1σ errors are dominated by the CO-to-H_2 conversion factor uncertainty (∼0.3 dex). We note that the error estimates of the millimeter continuum flux density, the CO(2–1) line velocity integrated intensity, and line luminosity consider a conservative NOEMA flux calibration uncertainty of 20% at 2 mm.

respectively. The sky annulus radii were set to 35″–45″ to minimize PSF wing contamination, and aperture corrections were also applied. From the SPIRE data, the sources flux density values or upper limits were computed following Savage & Oliver (2007). The Spitzer data were processed by Shi et al. (2014), who scaled the short–low (5–14 μm) spectrum, the long–low (14–40 μm) spectrum, and the overall flux of the spectrum to match the Spitzer MIPS 24 μm photometry. Shangguan et al. (2018) also found that the density flux scale of the Spitzer spectra were well matched with respect to the WISE data. The radio data were updated from those presented in Shangguan et al. (2018) considering newer literature data. We present the radio data in the Appendix.

2.3. Complementary AGN Sample

We complement our PG quasar CO survey with literature data taken from two main surveys, the BAT-AGN Spectroscopic Survey (BASS) sample presented in Koss et al. (2022) and the Close AGN Reference Survey (CARS; Husemann et al. 2022). In their data release 2, the BASS AGNs consist of 858 nearby ($z \lesssim 0.24$) AGNs selected by their ultrahard (14–195 keV) X-ray emission. We select a subsample of BASS AGNs presenting Hα and Hβ broad lines,[10] but we discard all the BASS AGNs with poor optical spectra models following Mejía-Restrepo et al. (2022). From this subsample, we further select host galaxies with CO(2–1) line emission detections or upper limits. Those BASS AGN host galaxies were observed with the Atacama Pathfinder Experiment telescope (APEX; 46 sources), the James Clerk Maxwell Telescope (JCMT; seven sources) and the Caltech Submillimeter Observatory (CSO; three sources). At the observed frequencies (∼220–229 GHz), the APEX, JCMT, and CSO observations have effective primary beam sizes of 26.″3–27.″5, 20.″4 and 32″, respectively, corresponding to scales of ∼6–27 kpc at the source redshifts (Koss et al. 2021). Specifically, we adopt the CO velocity integrated fluxes computed by fitting the line profiles with a single Gaussian or double-horn function. We note that Koss et al. (2021) show that those values are in good agreement with estimates computed by simply summing the CO emission over the line spectral range (see their Appendix D). The BASS AGN measurement uncertainties are 10% and 15% for flux calibration and aperture correction, respectively. We take the BASS AGN host galaxy properties from Koss et al. (2021). For the CARS survey, we take the AGN and host galaxy properties from Husemann et al. (2022) and Smirnova-Pinchukova et al. (2022), respectively. We note that the CO(2–1) line flux measurements were carried out using the IRAM 30 m telescope (Bertram et al. 2007). The IRAM 30 m telescope primary beam size is ∼10.″9–11.″4 at the observed frequencies (∼217–227 GHz), and correspond to physical scales ∼3–11 kpc. Bertram et al. (2007) estimate the CO line velocity integrated flux by simply summing the flux density over the full velocity range of the emission line. The IRAM 30 m telescope flux calibration uncertainty is ∼10%.

In consistency with the estimates presented for the PG quasars (Table 1), for both the BASS and CARS AGN surveys we use the AGN monochromatic luminosity at 5100 Å and broad Hβ line width values to estimate $L_{\rm bol}$ and $M_{\rm BH}$ following Richards et al. (2006) and Shangguan et al. (2018), respectively. The host galaxy CO luminosity and SFR values are estimated by using the conventions adopted in this work, and the stellar masses are scaled assuming the Kroupa (2001) initial mass function (IMF; see Section 3). The BH masses estimated by us and the values reported by Mejía-Restrepo et al. (2022) for the BASS AGNs are in good agreement, with an average BH mass ratio of ∼0.9 and 0.25 dex scatter. For the CARS sample there are several systems with fewer than two SED data points at $\lambda \gtrsim 60\ \mu$m, implying inaccurate far-IR emission luminosity estimates. Those correspond to 19 out of 38 host galaxies that were excluded whenever $L_{\rm IR}$ was involved in our analysis. On average, the discarded systems have slightly lower stellar masses (−0.2 dex) and CO(2–1) luminosities (−0.1 dex) compared to the full CARS sample, but present no systematic offsets in terms of the average molecular gas fraction, bolometric luminosity, BH mass, and Eddington ratio estimates (offsets $\lesssim$0.05 dex in terms of absolute values). However, we caution that by discarding those CARS host galaxies we may result with a subsample biased toward the most IR-luminous systems. The excluded CARS AGNs tend to be found at slightly higher redshifts ($z \approx 0.05$–0.06) compared

[10] Mejía-Restrepo et al. (2022) refer to those systems as Seyfert 1, 1.2, 1.5, and 1.8, based on the ratio between the broad Hβ and [O III] line luminosities. Here, we only refer to those BASS AGNs as "Sy1–1.8."

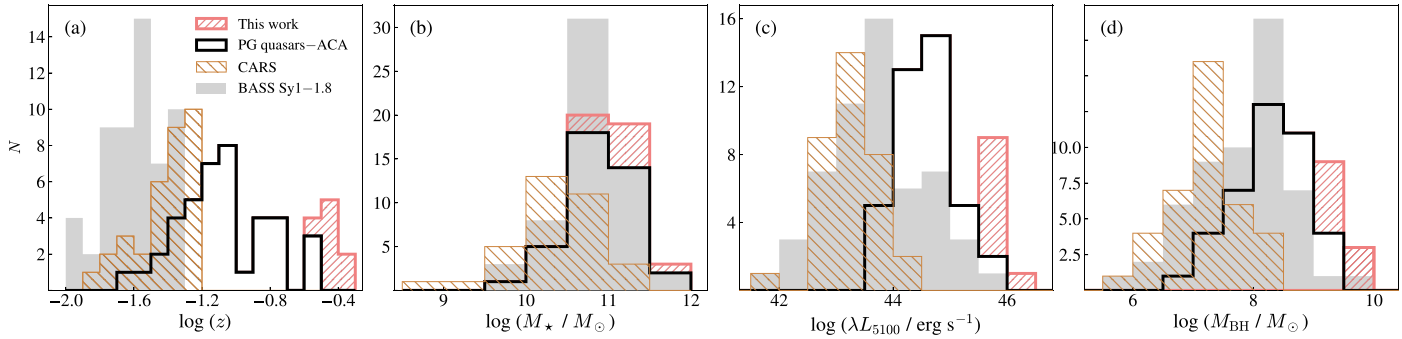

Figure 2. Comparison between our target sample (red) with the sample of PG quasars with previously detected CO emission (black; Shangguan et al. 2020b), the BASS type 1 AGN subsample (gray), and the CARS survey (brown), in terms of (a) redshift, (b) host galaxy stellar mass, (c) 5100 Å AGN luminosity, and (d) BH mass. Our target sample is presented over the "PG quasar–ACA" sample data to improve figure visualization.

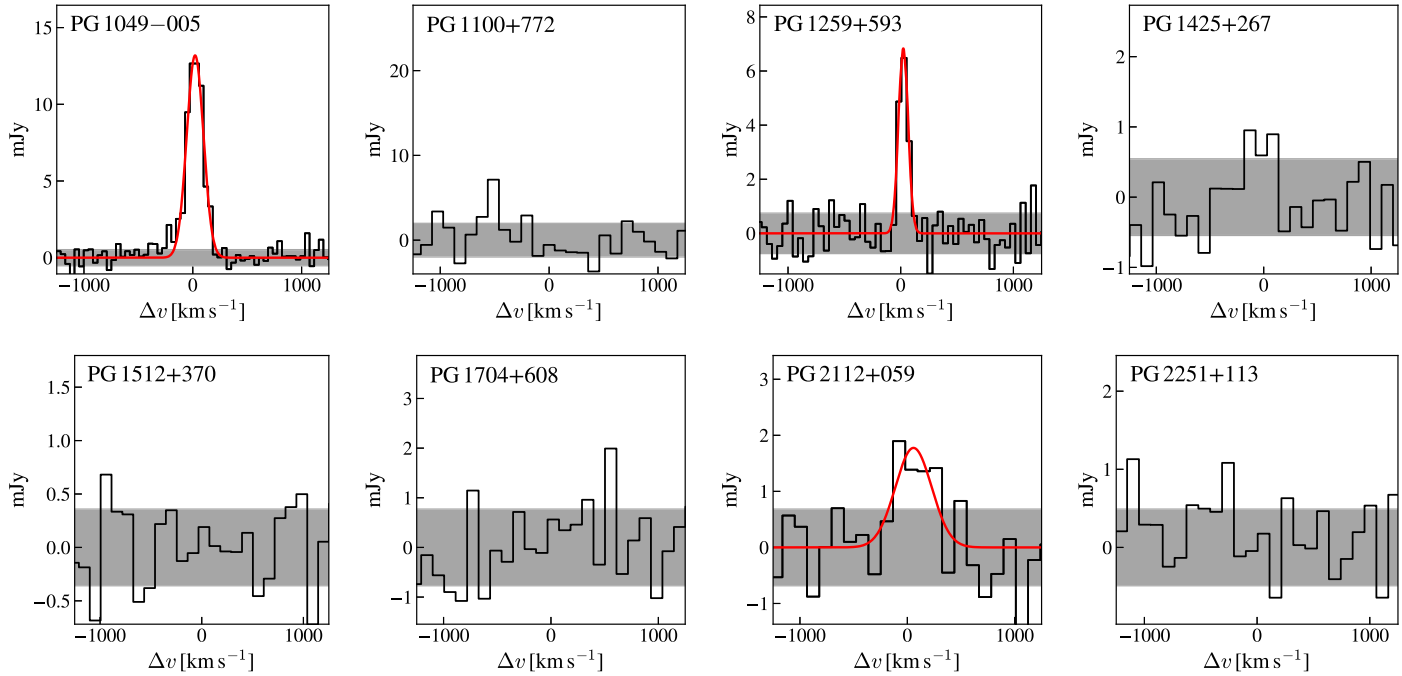

Figure 3. Spectra at rest-frame ∼1.3 mm of the eight PG quasar host galaxies. The red curve corresponds to the best-fit Gaussian model. The gray shade highlights the spectrum $\pm1\sigma$ level, with σ representing the rms of emission-line-free channels. In the cases where no CO(2–1) emission is detected, the spectrum is centered at the expected line location following the redshift derived from optical light.

to the sample average ($\langle z \rangle \approx 0.04$). We further exclude few duplicated objects among the BASS, CARS, and PG quasar surveys.

Figure 2 presents the properties of our sample, i.e., PG quasars with previous CO line measurements (Shangguan et al. 2020b), forming a subsample of broad-lined BASS AGNs and CARS targets. The BASS subsample corresponds to 56 $z \lesssim 0.05$ host galaxies (21 upper-limit estimates). The CARS subsample consists of 34 $z \lesssim 0.06$ systems (nine upper-limit estimates). The PG quasars and BASS AGNs cover similar host galaxy stellar mass ranges, while the CARS host galaxies tend to be less massive. Compared to those three AGN samples, our targets tend to be slightly biased toward the more massive systems in terms of stellar mass, expected as we selected local quasars with the most massive BHs, and hence the host galaxies presenting the most massive bulges. The sample of eight PG quasars presented here probes the high BH mass and AGN luminosity tails of the $z \lesssim 0.5$ AGN population.

3. Methods

3.1. CO(2–1) Emission-line and Millimeter Continuum Characterization

To estimate the CO(2–1) velocity integrated intensity, first, we get a spectrum by spatially collapsing the data cube within a beam-sized region centered at the expected target location (Figure 3). This aperture selection was set after exploring different values aiming to maximize the CO line S/N detection, and roughly corresponds to the host galaxy stellar component size reported by Zhao et al. (2021). Then, we fit the line emission by simply using a Gaussian function deriving the line velocity integrated intensity ($S_{CO}\Delta v$), center (ν_{obs}), and FWHM. We quantify the total continuum flux density (S_{cont}) by simply fitting a two-dimensional Gaussian model to the continuum image (Figure 4). We found a good agreement between S_{cont} and the continuum flux density values estimated by summing the individual pixel values within an aperture of

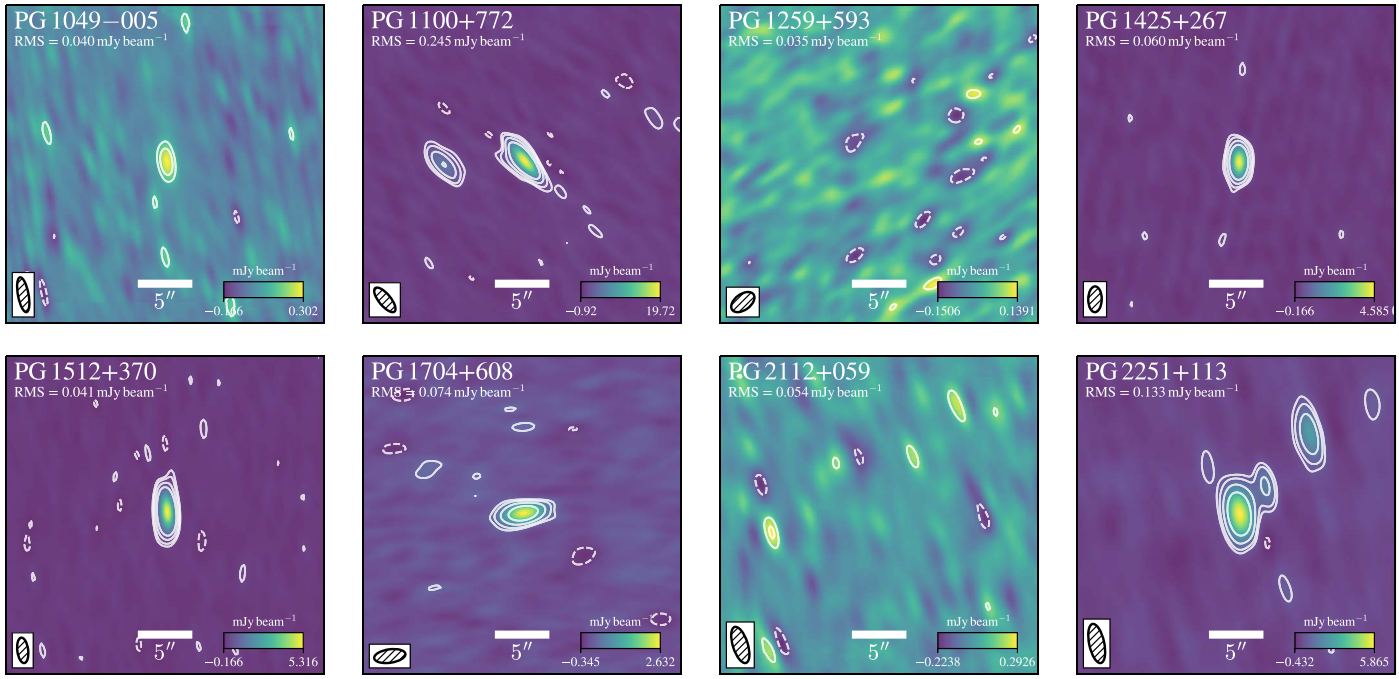

Figure 4. Continuum images at rest-frame ∼1.3 mm for the PG quasar hosts. The contours indicate −3 (dashed), 3, 5, 10, and 20σ levels, with σ being the rms value of source-free pixels and indicated in each map. The synthesized beam is shown in the lower-left corner of each image.

20″ (similar to that used for the Herschel data) centered on the continuum peak location (average ratio ∼1.08, scatter ∼0.23 dex). In both cases, we estimate the uncertainties by resampling the data in 1000 iterations using the rms of the residuals as the noise level. The 1σ errors are obtained from the distributions build for each parameter. In the case of nondetection, the CO(2–1) emission line and continuum 3σ upper limits were calculated as

$$S_{\rm CO}\Delta v < 3\sigma_{\rm CO}\,\delta v\,\sqrt{N_{\rm ch}\frac{N_{\rm A}}{N_{\rm B}}}, \quad (1)$$

and

$$S_{\rm cont} < 3\sigma_{\rm cont}\,\sqrt{\frac{N_{\rm A}}{N_{\rm B}}}, \quad (2)$$

respectively, where $\sigma_{\rm CO}$ is the rms level of the data cube, δv is the velocity resolution, $N_{\rm ch}$ is the number of channels sampling the CO line FWHM (assumed to be 400 km s^{-1} given the stellar masses of our targets and the $M_\star$–FWHM trend reported by Shangguan et al. 2020b for local PG quasars), $N_{\rm A}$ is the aperture size in pixel units, and $N_{\rm B}$ is the number of pixels for the synthesized beam. We assume $N_{\rm A} = 3N_{\rm B}$ for estimating the CO flux density upper limits (Hainline et al. 2004; Michiyama et al. 2021), while $N_{\rm A} = 20''$ for the continuum. We list the estimates (or upper limits) for each source in Table 3.

The CO(2–1) line luminosity is calculated following (Solomon & Vanden Bout 2005)

$$L'_{\rm CO(2-1)} = 3.25\times10^7\,\frac{S_{\rm CO(2-1)}\Delta v\,D_L^2}{\nu_{\rm obs}^2(1+z)^3}\ [{\rm K\,km\,s^{-1}\,pc^2}], \quad (3)$$

where $S_{\rm CO(2-1)}\Delta v$ is in units of Jy km s^{-1}, D_L is the luminosity distance in Mpc, $\nu_{\rm obs}$ is the observed frequency of the line in GHz, and z is the redshift. We estimate the luminosity of the CO(1–0) line transition ($L'_{\rm CO(1-0)}$) by adopting the median luminosity ratio $r_{21} \equiv L'_{\rm CO(2-1)}/L'_{\rm CO(1-0)} = 0.62$ found by Shangguan et al. (2020b) for PG quasars at $z < 0.3$.[11] The molecular gas masses are estimated under the assumption of $\alpha_{\rm CO} = 3.1\ M_\odot\ ({\rm K\,km\,s^{-1}\,pc^2})^{-1}$, as suggested by the comparison of $L'_{\rm CO(1-0)}$ and the dust-based gas masses for the $z < 0.3$ PG quasars (Shangguan et al. 2020b), and in consistency with the recommendation by Sandstrom et al. (2013) for nearby star-forming galaxies.

3.2. Far-IR SED Modeling and IR-based SFRs

We use our $S_{\rm cont}$ estimates to complement the far-IR SED (Section 2.2) and update the AGN-decontaminated IR luminosity values previously estimated by Shangguan et al. (2018) for our targets. Our $S_{\rm cont}$ measurements provide key information for constraining the targets far-IR SED flux density at low frequencies.

Shangguan et al. (2018) modeled the far-IR SED by adopting physically motivated emission components for the AGN dusty torus, host galaxy cold dust, and starlight. The torus emission is modeled by using the CLUMPY model (Nenkova et al. 2008a, 2008b), plus a complementary blackbody component that accounts for emission from the torus of very hot dust (Zhuang et al. 2018). The far-IR models adopt a fixed dust emissivity index (β) within the Draine & Li (2007) models (roughly $\beta \approx 2.08$). The far-IR modeling also handles a synchrotron emission component, but its addition to the SED is optional, depending on the radio data availability. The

[11] For the BASS AGNs Lamperti et al. (2020) report an average $r_{21} = 0.72$ value, with a median absolute deviation of 0.17. For the CARS sample, we use the CO(1–0) and CO(2–1) velocity integrated intensity values provided by Bertram et al. (2007) for 25 sources and estimate a median value of $r_{21} = 0.61^{+0.34}_{-0.17}$.

synchrotron emission is modeled as a power-law spectrum with a fixed spectral index ($S_\nu \propto \nu^{\alpha_R}$). A 5 Gyr stellar population with a Kroupa (2001) IMF from Bruzual & Charlot (2003) is assumed for the starlight component. We refer to Shangguan et al. (2018), for more details. The SED data and models are presented in Figure 5.

We compute the IR luminosity by integrating the host galaxy far-IR SED subcomponent corresponding to the cold dust emission and over 8–1000 μm (Table 3). To estimate the SFR, we use Kennicutt (1998)'s calibration, renormalized to a Kroupa (2001) IMF

$$\mathrm{SFR}(M_\odot\ \mathrm{yr}^{-1}) = 3 \times 10^{-44}\, L_{\mathrm{IR}}(\mathrm{erg\ s}^{-1}). \quad (4)$$

We note that the systematic uncertainties of the far-IR SED model decomposition dominate the SFR errors. Xie et al. (2021) found that IR-based SFRs correlate with estimates from mid-IR neon emission lines with ∼0.2–0.3 dex scatter for $z < 0.3$ PG quasar hosts.[12] Hereafter, we assume this scatter value as the 1σ error of our SFR estimates.

4. Results

Our main goal is to study whether AGNs may affect the cold molecular gas content in a sample of the most powerful unobscured quasars observed at low-z. From the subsample of eight quasars presented in this work, we detect CO(2–1) emission coming from three host galaxies (Figure 3). Those three systems tend to have less-massive BHs and higher Eddington ratios among the sample of eight objects. Considering both the NOEMA and ACA campaigns, we detect line emission in 36 out of 48 host galaxies. All 17 disk-like host galaxies are detected in CO, while we detect CO emission in seven out of nine merger systems, and in five ellipticals from a total of 12 (five nondetections from this campaign). We detect CO emission in 7/10 host galaxies with uncertain morphology classifications. Using the qualitative radio spectra classification for the PG quasars (Shangguan et al. 2018), we find that 33/38 radio-quiet systems are detected in CO, three out of four PG quasars with flat radio spectra present line detections, and no CO emission was detected in systems with steep radio spectra (six in total).

Thanks to the large frequency coverage of NOEMA, we detect the rest-frame ∼1.3 mm continuum in six systems (Figure 4). The modeling of the global far-IR SEDs (Figure 5) suggests that the rest-frame ∼1.3 mm continuum can be associated with synchrotron emission from a jet in five sources. We now proceed to analyze the data in detail.

4.1. Total Gas Mass Content Estimated from Cold Dust Emission

The far-IR SED of a galaxy can be used to predict the dust mass, which is closely related to the total gas content (Draine et al. 2007; Leroy et al. 2011). Shangguan et al. (2018) provided total gas mass (M_{gas}) estimates for PG quasar host galaxies, finding that those closely correlate with direct measurements from CO emission plus atomic gas (H I) for the closer systems. Here, we extend their analysis by comparing both the molecular gas masses estimated from the CO(2–1) emission-line luminosity and M_{gas} values for the $z < 0.5$ PG quasar host galaxy sample. The latter quantity is computed by converting the dust masses to M_{gas} using the dust-to-gas ratio values derived by Shangguan et al. (2018), but avoiding the correction factor (∼0.23 dex) for extended atomic hydrogen gas content ($M_{\mathrm{gas,sub}}$). Hence, the $M_{\mathrm{gas,sub}}$ estimates correspond to the atomic plus molecular gas mass within roughly the same host galaxy area where the dust emission originates (Shangguan et al. 2018). The M_{gas} values have a systematic uncertainty of ∼0.2 dex, while the CO-based estimates have a typical uncertainty of ∼0.32 dex inherent to α_{CO} (∼0.3 dex), and R_{21} (∼0.1 dex). We remind the reader that the $L'_{\mathrm{CO\ (2-1)}}$ uncertainty is dominated by the flux calibration uncertainties.

Figure 6 shows $M_{\mathrm{H_2}}$ against $M_{\mathrm{gas,sub}}$ for the full sample of PG quasars (NOEMA plus ACA campaigns). Both quantities closely match, in agreement with the previous finding of Shangguan et al. (2018; their Figure 10). We compute a mean $M_{\mathrm{H_2}}/M_{\mathrm{gas,sub}}$ ratio of 0.93 with a scatter ∼0.40 dex. The scatter is consistent with the mass ratio systematic uncertainty (∼0.38 dex), but we note that it may be larger considering the $M_{\mathrm{H_2}}$ upper limits. Among the PG quasars, the disk-like host galaxies present an average $M_{\mathrm{H_2}}/M_{\mathrm{gas,sub}} \approx 0.95$ and scatter slightly reduced to 0.32 dex. $M_{\mathrm{gas,sub}}$ tends to be larger than $M_{\mathrm{H_2}}$ in mergers. For such systems, the data average ratio and scatter is 0.80 and 0.23 dex, respectively; however, we caution the low statistics (seven host galaxies). We only detect CO emission in five elliptical host galaxies, so we do not provide any statistical measurement. For the PG quasar hosts with uncertain morphological classification, we find an average mass ratio of 0.77, with scatter ∼0.51 dex. Our sample is too small to characterize statistically the subsample of PG quasar host galaxies presenting a flat or steep radio spectrum. The radio-quiet quasars are characterized by an average $M_{\mathrm{H_2}}/M_{\mathrm{gas,sub}} \approx 0.92$, with a scatter of 0.37 dex. Our observations suggest low atomic gas content inside the stellar disks of the PG quasar host galaxies, but this result sensibly depends on the correction factor applied to the dust-to-gas ratio, namely the extended H I mass value subtracted to M_{gas}. Only 13 PG quasars hosts have H I global measurements from literature, most of these host galaxies are ongoing mergers where the emission lines exhibit complex profiles and suggest dynamical disturbance, or have neighboring companions (e.g., PG 0007+106 and PG 1119+120) inducing signal confusion (Shangguan et al. 2018). Detailed observations resolving the H I content in PG quasars hosts are needed to draw deeper conclusions.

4.2. AGN Properties Compared to $L'_{\mathrm{CO(2-1)}}$

We compare the CO(2–1) luminosity with respect to λL_{5100} and the Eddington ratio in Figure 7 for the PG, BASS, and CARS type 1 AGNs. We use `pymccorrelation` (Privon et al. 2020) to compute the generalized Kendall's rank correlation coefficient (τ) considering the censored data (Isobe et al. 1986). We assume $p \leqslant 0.05$ to determine if the quantities are correlated. We find that the CO luminosity does not correlate with the Eddington ratio with $\tau = 0.09$ and a p-value of 0.10. This is consistent with the results from the previous ACA campaign targeting PG quasar hosts (Shangguan et al. 2020a), but inconsistent with the findings of Koss et al. (2021), who found a tentative increase of molecular gas mass (hence, $L'_{\mathrm{CO(2-1)}}$) with Eddington ratio for the full BASS AGN sample (their Figure 15). Nevertheless, Koss et al. (2021) analyzed

[12] While Xie et al. (2021) analyzed the full sample of $z < 0.5$ PG quasars with Herschel data (Shangguan et al. 2018), the most distant host galaxy detected in mid-IR neon emission is at $z \approx 0.32$ (PG 2251+113).

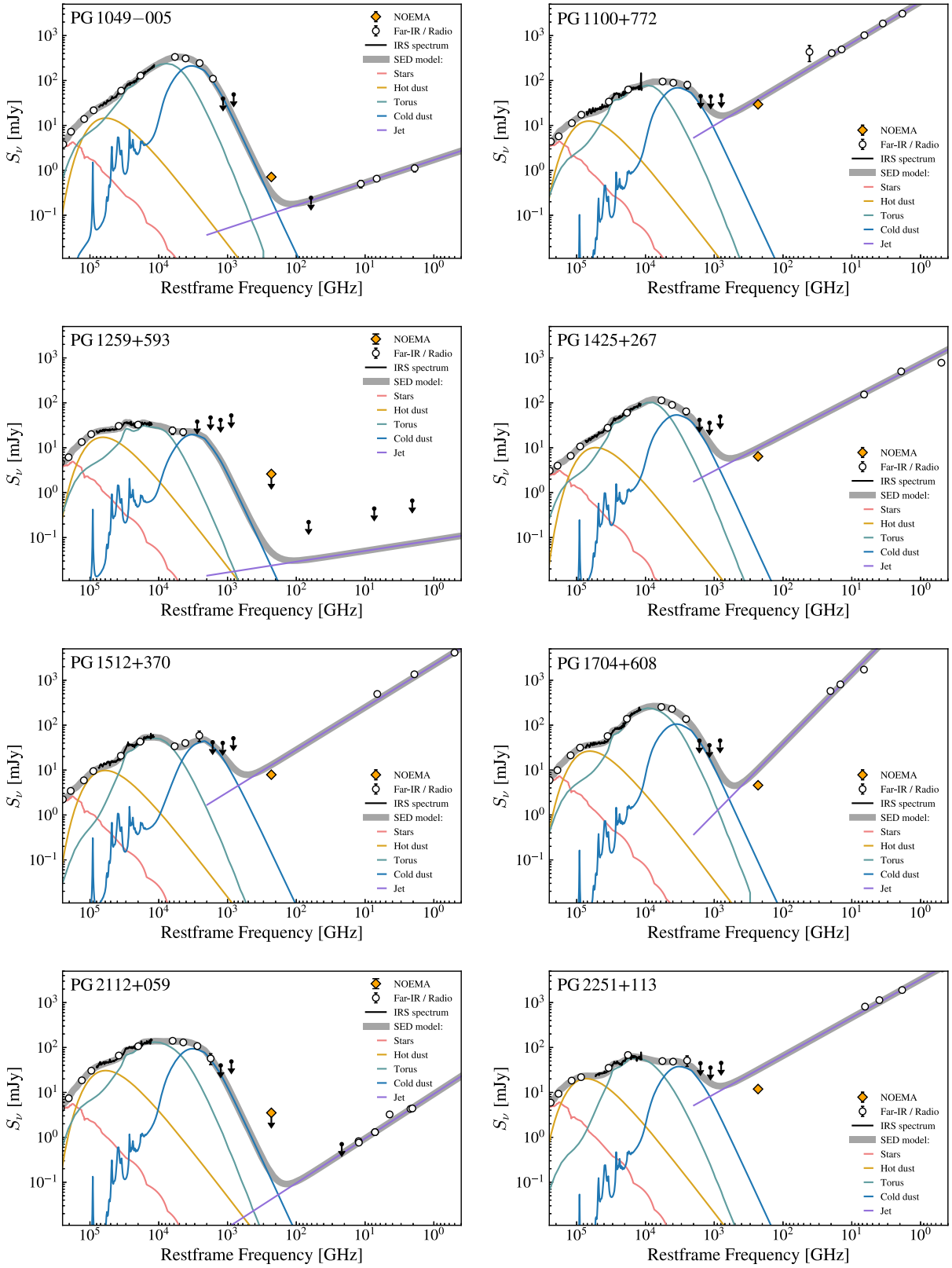

Figure 5. Far-IR SEDs of the eight PG quasar host galaxies. The orange diamonds indicate the NOEMA ∼2 mm continuum. The open circles show the IR data from 2MASS, WISE, and Herschel collated in Shangguan et al. (2018; see Section 2.2), along with the GHz radio data taken from the literature. Upper limits are indicated by downward arrows (see the Appendix). The black solid line represents the available IRS spectrum in the ∼5–40 μm wavelength range. The far-IR SED model is the gray band, and it is composed by five subcomponents: starlight (red), hot dust (yellow), AGN torus (green), cold dust (blue), and jet (purple; Section 3.2).

type 1 and type 2 AGNs, while we only analyze type 1 AGNs. We find that $L'_{\rm CO(2-1)}$ and λL_{5100} are weakly correlated ($\tau = 0.18$, $p < 0.01$). This result agrees with that reported by Shangguan et al. (2020a), but the correlation coefficient is ∼2 times lower due to the inclusion of the less-luminous BASS and CARS AGNs.

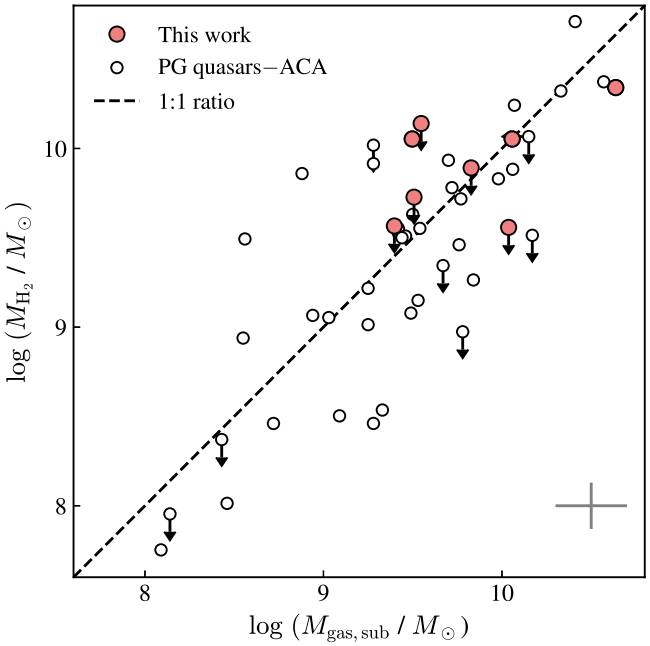

Figure 6. CO-based molecular gas mass compared to the total gas mass predicted from cold dust emission and subtracted for extended atomic gas (H I) content. In the bottom right corner we present the typical 1σ uncertainty of the data. The arrows denote 3σ upper limits.

We also provide median trends by computing median values over bins of 1.0 dex in λL_{5100} and 0.6 dex in $L_{\rm bol}/L_{\rm Edd}$ using the Kaplan–Meier estimator implemented in the `Python` package `lifelines`,[13] including CO(2–1) upper limits. The median trend between $L'_{\rm CO(2-1)}$ and $L_{\rm bol}/L_{\rm Edd}$ is nearly constant, as expected because both quantities are not correlated. In terms of $L'_{\rm CO(2-1)}$ and λL_{5100}, the median trend suggests an $\sim$0.4 dex increase of $L'_{\rm CO(2-1)}$ for AGNs with $\lambda L_{5100} \gtrsim 10^{44}$ erg s^{-1}. Such an increase of $L'_{\rm CO(2-1)}$ with λL_{5100} is not artificially produced by host galaxy mass selection bias as most of these AGNs tend to be hosted in galaxies with $M_\star \approx 10^{10.75}$–$10^{11.5}\,M_\odot$. We note that the AGNs with $\lambda L_{5100} \lesssim 10^{44}$ erg s^{-1} tend to be observed in the nearby universe ($z \lesssim 0.1$), while the more-luminous quasars with $\lambda L_{5100} \approx 10^{46}$ erg s^{-1} tend to be found at higher redshifts ($\langle z \rangle \approx 0.35$) where galaxies have molecular gas fractions ($f_{\rm H_2} \equiv M_{\rm H_2}/M_\star$) about twice higher than local ones (Tacconi et al. 2018), meaning that the possible increase of $L'_{\rm CO(2-1)}$ with λL_{5100} could be due to the cosmic evolution of the molecular gas content in galaxies.[14] To test this possibility, we correct the host galaxy CO(2–1) luminosity by adopting the parameterization of Tacconi et al. (2018) for the cosmic evolution of $f_{\rm H_2}$ for main-sequence galaxies and a constant $\alpha_{\rm CO}$ value. In this case, we find no correlation between the corrected $L'_{\rm CO(2-1)}$ and λL_{5100} ($\tau = 0.11$, $p = 0.06$).

4.3. The $L_{\rm IR} - L'_{\rm CO(2-1)}$ relation

In Figure 8 we show the relation between $L_{\rm IR}$ and $L'_{\rm CO(2-1)}$ for the AGNs in our sample. We find that the more powerful quasars observed in this work ($\lambda L_{5100} \gtrsim 10^{45.5}$ erg s^{-1}) follow the best-fit relation of Shangguan et al. (2020a; their Equation (4), after correcting by R_{21}). The five systems with $L'_{\rm CO(2-1)}$ upper limits provided by NOEMA tend to be on or above the best-fit relation of Shangguan et al. (2020a), suggesting even lower $L'_{\rm CO(2-1)}$ values. However, we caution that due to the presence of strong synchrotron emission and Herschel photometry upper limits, their $L_{\rm IR}$ estimates are somewhat more uncertain than for the rest of our targets.

Surprisingly, we find that the BASS sample of type 1 AGNs is in offset with respect to the $L_{\rm IR} - L'_{\rm CO(2-1)}$ best fit provided by Shangguan et al. (2020a) for the PG quasars. We quantify this offset $= -0.54$ dex in terms of $L_{\rm IR}$. We report a similar result when including the BASS type 2 AGN data (not shown). The CARS host galaxies follow a trend similar to that reported for the PG quasars, but this result could be affected by IR luminosity bias induced when discarding the systems with poorly sampled far-IR SED. The redshift difference between the BASS AGN and PG quasar samples is not high enough to explain this offset. Among the PG quasar sample, 13 out of 48 host galaxies are at $z \sim 0.05$, similar to the BASS AGN systems, while 27 PG quasar host galaxies are at $z \lesssim 0.1$, making these practically immune to any cosmic evolutionary effect. We also note that the offset for the BASS type 1 AGNs cannot be explained by incorrect aperture correction when deriving the CO(2–1) luminosity (Koss et al. 2021). The NOEMA- and ACA-based CO(2–1) emission-line measurements for the PG quasars do not suffer from any systematics in aperture (Shangguan et al. 2020a). Nor does the offset arise from the use of different far-IR SED models when estimating $L_{\rm IR}$. The PG quasar far-IR modeling is detailed in Section 3.2, and here we only highlight that this method is consistent with fitting a modified blackbody (MBB) to the far-IR SED (see the Appendix of Shangguan et al. 2018). For the BASS sample, the far-IR luminosities were computed mainly by Shimizu et al. (2017), with some few systems taken from Ichikawa et al. (2019). Both methods are consistent between each other (see the Appendix of Shimizu et al. 2017). We fitted the far-IR SEDs of our targets following the method outlined in Shimizu et al. (2017), namely by considering a MBB plus an additional subcomponent modeling the emission from the warm dust heated by the AGN and intense star formation activity. We found no significant discrepancy between the $L_{\rm IR}$ values provided by those fits and the estimates reported in Table 3, notwithstanding a scatter of 0.2 dex. For the CARS sample, we obtain similar results when comparing the IR luminosity reported by Smirnova-Pinchukova et al. (2022) and the result of our MBB fits. Therefore, we find that the BASS AGNs tend to be offset with respect to the PG sample in the $L_{\rm IR} - L'_{\rm CO(2-1)}$ plane.

Compared to the inactive systems, represented by the fits for normal star-forming galaxies and starbursts (Genzel et al. 2010), the less-luminous PG quasars follow the relation of starbursts (Shangguan et al. 2020a, 2020b). The same picture holds for the most-luminous PG quasars at $z \lesssim 0.5$. The subsample of BASS type 1 AGNs follows the relation of normal star-forming galaxies.

4.4. Molecular Gas Fraction and Depletion time

Figure 9 shows the molecular gas fraction as a function of λL_{5100} and Eddington ratio. We find no significant correlation between $f_{\rm H_2}$ and λL_{5100} ($\tau = 0.05$, p-value $= 0.37$). This result does not change after taking into account the host galaxy

[13] https://lifelines.readthedocs.io/en/latest/index.html#

[14] There is no significant bias with host galaxy redshift when considering the Eddington ratio estimates.

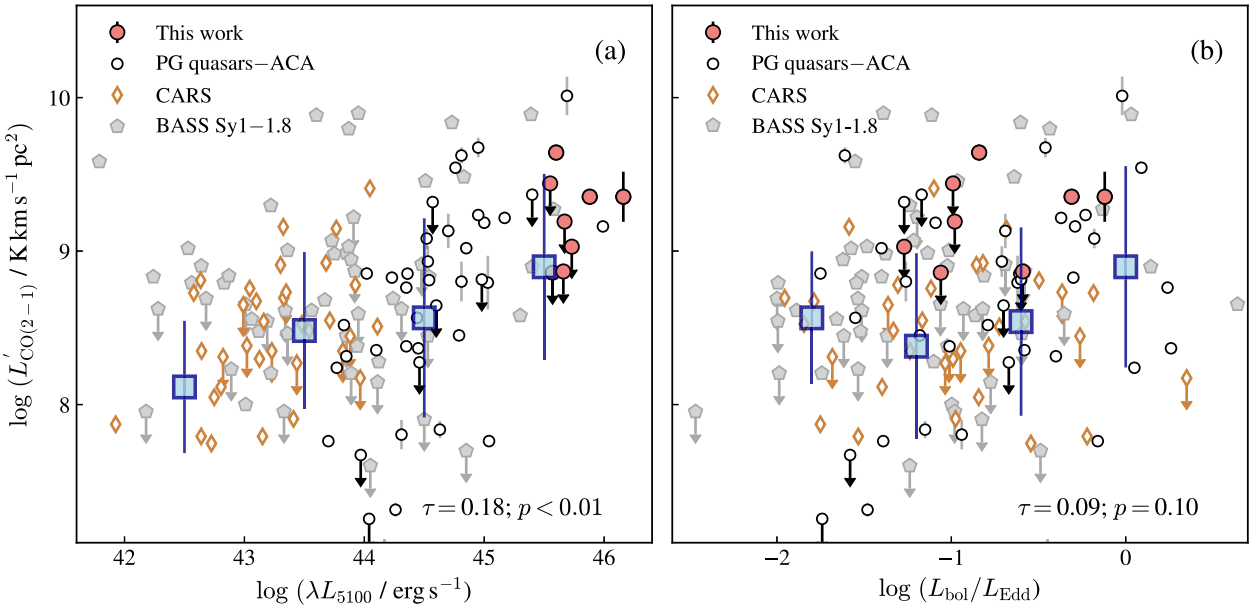

Figure 7. The dependence of CO luminosity on (a) λL_{5100} and (b) Eddington ratio. In both panels, the blue squares correspond to median $L'_{\rm CO(2-1)}$ values computed in 0.6 dex λL_{5100} and 0.3 dex $L_{\rm bol}/L_{\rm Edd}$ bins. The arrows correspond to 3σ upper limits.

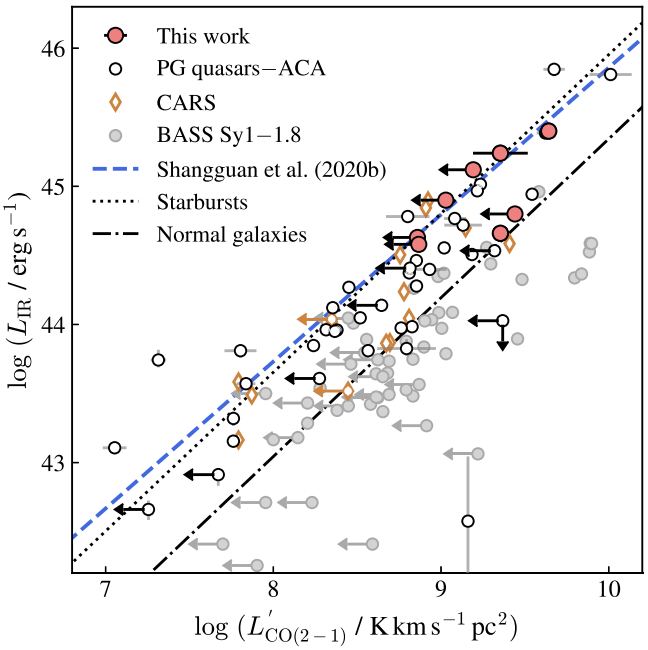

Figure 8. IR luminosity as a function of CO(2–1) line luminosity. The arrows denote 3σ upper limits. The best fit of Shangguan et al. (2020b) has a slope consistent with unity and an intrinsic scatter of ∼0.3 dex. The trends for inactive systems correspond to those reported in Genzel et al. (2010) for normal star-forming systems (0.33 dex scatter) and starbursts (0.21 dex scatter).

redshift bias with λL_{5100} ($\tau = -0.07$, p-value $= 0.21$). The constant $f_{\rm H_2}$–λL_{5100} median trend further highlights this. On the other hand, we find a weak correlation between $f_{\rm H_2}$ with Eddington ratio ($\tau = 0.14$, p-value $= 0.02$), but the corresponding $f_{\rm H_2}$–Eddington ratio median trend does not suggest any significant correlated increase.

Figure 9 also presents the depletion time ($t_{\rm dep} \equiv M_{\rm H_2}/{\rm SFR}$) as a function of λL_{5100} and Eddington ratio. We find no correlations with λL_{5100} ($\tau = -0.08$, p-value $= 0.18$) or Eddington ratio ($\tau = -0.06$, p-value $= 0.30$). Considering the depletion time cosmic evolution (Tacconi et al. 2018) has a negligible effect on the correlation coefficient values. If anything, the $t_{\rm dep}$–$L_{\rm bol}/L_{\rm Edd}$ median trend suggests a somewhat minor $t_{\rm dep}$ decrease from ∼1.0 to ∼0.4 Gyr at $L_{\rm bol}/L_{\rm Edd} \gtrsim 0.1$, but note that the median trend may only reflect the Eddington ratio range at which the CARS and PG quasar sample dominate the median bin statistics.

5. Discussion

The properties of the molecular gas in AGN host galaxies provide important clues regarding the role of BH accretion in shaping the evolution of galaxies. Early studies already suggested that local luminous quasars are hosted in galaxies with significant gas reservoirs (Scoville et al. 2003; Evans et al. 2006; Bertram et al. 2007). These findings were subsequently supported by many new observations detecting CO emission for broader samples of local type 1 and type 2 AGNs (Husemann et al. 2017; Rosario et al. 2018; Shangguan et al. 2020b; Koss et al. 2021; Ramos Almeida et al. 2022; Salvestrini et al. 2022). The large amounts of cold gas content detected in type 1 AGN hosts are at odds with the idea of negative AGN feedback affecting the host galaxies globally (e.g., Husemann et al. 2017; Jarvis et al. 2020; Shangguan et al. 2020a; but see Ellison et al. 2021; Ward et al. 2022), with conflicting results regarding how the AGN properties correlate with the molecular gas properties in AGN host galaxies. Koss et al. (2021) reported that the BASS AGNs with higher Eddington ratio tend to have on average larger molecular gas reservoirs, which disagrees with the findings of Shangguan et al. (2020a) who report that the CO luminosity does not correlate with Eddington ratio for local PG quasars (see also Husemann et al. 2017). This disagreement seems to arise because both samples are complementary in terms of AGN luminosity, with the PG quasars representative of more-luminous AGNs (Figure 2). It should be noted that Shimizu et al. (2016) already suggested that the BASS AGN sample may not extend to high enough AGN luminosity to reveal correlations with the host galaxy properties. Conversely,

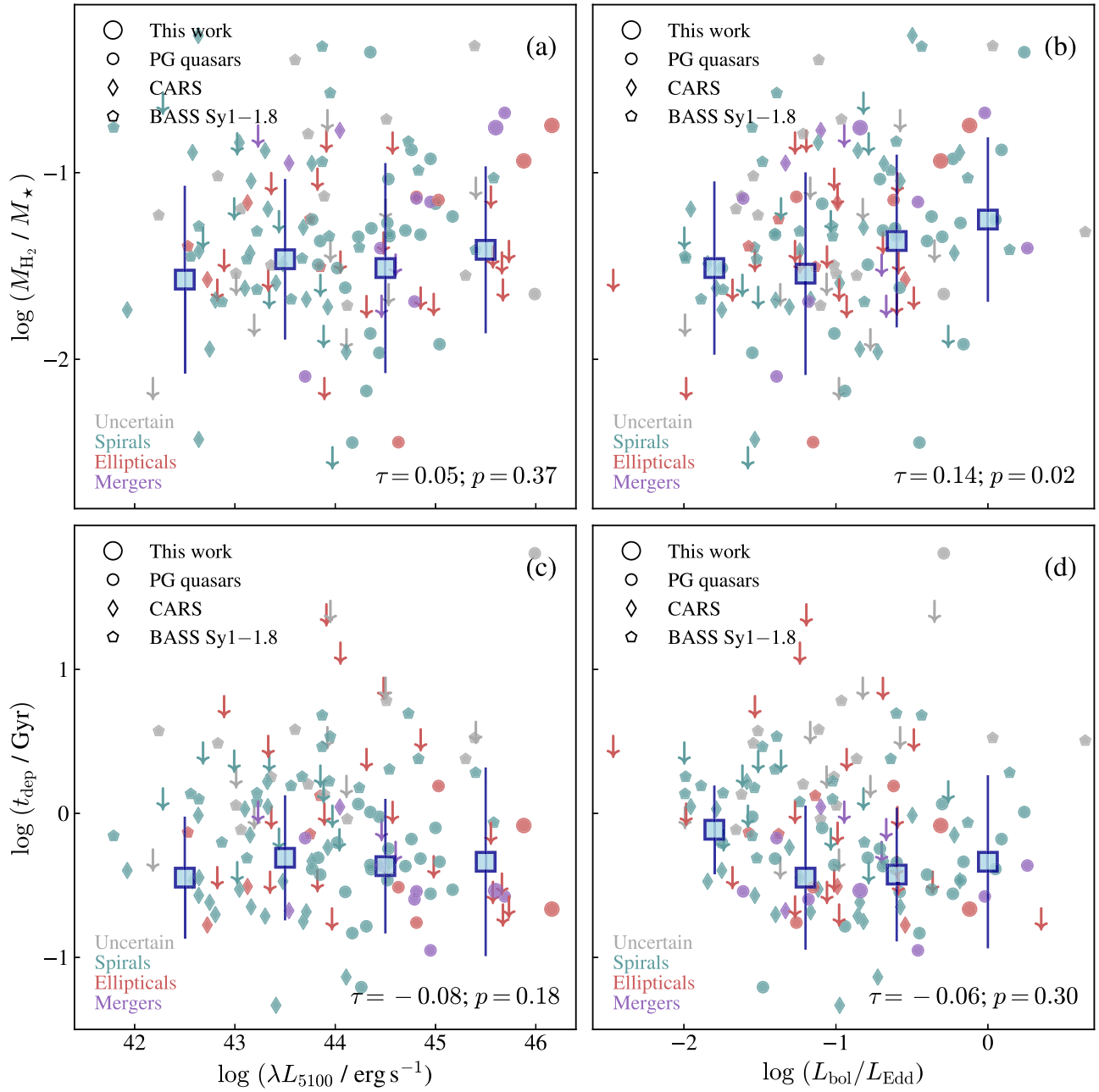

Figure 9. Host galaxy molecular gas properties as a function of AGN properties. The molecular gas fraction ($M_{H_2}/M_\star$) dependence with (a) λL_{5100} and (b) Eddington ratio. Panels (c) and (d) show similar dependences on AGN properties, but for the molecular gas depletion time (M_{H_2}/SFR). In all panels, the data are colored by host galaxy morphology, and the blue squares correspond to median $M_{H_2}/M_\star$ or t_{dep} values computed in 0.6 dex λL_{5100} and 0.3 dex L_{bol}/L_{Edd} bins, respectively. The arrows correspond to 3σ upper limits.

artificial correlations between host galaxy and AGN properties could also arise because of sample selection biases, with targets covering a narrow range in terms of AGN properties (Zhuang & Ho 2020). When combining the BASS type 1 AGNs, CARS, and the PG quasar samples, including our observations, we further confirm the lack of correlation between CO luminosity (i.e., molecular gas mass) with Eddington ratio, in agreement with Husemann et al. (2017) and Shangguan et al. (2020a). On the other hand, we find a weaker correlation between CO emission and AGN luminosity than that reported by Shangguan et al. (2020a), mainly because of the inclusion of the less-luminous BASS and CARS AGN data in the analysis. This correlation is mainly driven by the more-luminous AGNs ($\lambda L_{5100} \gtrsim 10^{45}$ erg s^{-1}) observed at higher redshift, and it vanishes when correcting the CO luminosity by the cosmic evolution of the molecular gas content in galaxies. The observed trends suggest a lack of negative AGN feedback effects on the molecular gas content of the host galaxies.

Even though we report a lack of correlation between $L'_{CO(2-1)}$ and λL_{5100} for the full sample of type 1 AGNs (after correcting for redshift), we note that there is still a stronger link remaining for the PG quasar sample alone (Shangguan et al. 2020a). Such a trend is reminiscent of that found between AGN luminosity and SFR for local AGNs, where the processes that drive and regulate most of the star formation in low-luminosity AGN hosts presumably do not strongly affect BH fueling, while in high-luminosity AGNs it may be the opposite (Rosario et al. 2012). If there is any correspondence between the global

SFR and BH accretion events in high-luminosity AGNs, it should occur over timescales short compared to the AGN duty cycle (∼10–100 Myr; Hopkins et al. 2005), requiring that most of the star formation activity being triggered in the central region of the host galaxies. Under this scenario, the $L'_{\rm CO(2-1)} - \lambda L_{5100}$ trends reported for the full sample of type 1 AGNs and PG quasar sample alone may reflect how differently the gas is distributed within the PG quasar hosts compared with the BASS AGN host galaxies, in addition to a closer connection between the AGN properties and the molecular gas content on the central scales of the quasar hosts. Note that the more gas-rich PG quasars have compact molecular gas distributions (Molina et al. 2021). In AGN hosts, the cold dust emission mainly arises from compact nuclear scales (Mushotzky et al. 2014; Lutz et al. 2018; Molina et al. 2023). Additionally, our $L_{\rm IR}/L'_{\rm CO}$ measurements for the BASS AGNs and PG quasars presume a difference in the gas distribution between both type 1 AGN samples. Similarly to Bertram et al. (2007), we find that type 1 AGNs can be roughly separated into two populations in terms of $L_{\rm IR}/L'_{\rm CO}$ (a proxy of the star formation efficiency or $t_{\rm dep}$), with one population, most of the BASS AGNs, following the typical $L_{\rm IR}/L'_{\rm CO}$ ratio found in normal star-forming galaxies, and a second population, the PG quasars, and some CARS AGNs, presenting $L_{\rm IR}/L'_{\rm CO}$ values comparable to those measured for luminous IR galaxies (Figure 8). It is well known that luminous IR galaxies have molecular gas distributions mainly concentrated in their central kiloparsec and subkiloparsec regions (e.g., Downes & Solomon 1998; Iono et al. 2009; Bellocchi et al. 2022), while normal star-forming galaxies have more extended gas distributions (e.g., Bolatto et al. 2017). Accounting for the difference in gas distribution for both type 1 AGN samples would imply adopting different r_{21} and CO-to-H_2 conversion factor values when estimating the host galaxy molecular gas masses, further decreasing the $M_{\rm H_2}$ values for the PG quasars, and amplifying both AGN sample differences in terms of $t_{\rm dep}$ or star formation efficiency.

Recent findings suggest that more-luminous and more efficiently growing BHs tend to be hosted in starbursts (Bernhard et al. 2016; Shangguan et al. 2020a; Xie et al. 2021). The position of an AGN host relative to the main sequence of star-forming galaxies seems to be correlated with Eddington ratio (e.g., Ellison et al. 2016; Shimizu et al. 2016; Woo et al. 2020; Zhuang & Ho 2020, 2022; Torbaniuk et al. 2021). How does BH accretion connect to the galaxy's star formation activity on much larger scales? A straightforward possibility is the common dependence of BH growth and star formation on the molecular gas supply (Jarvis et al. 2020; Shangguan et al. 2020b), replenished by gravitational instabilities that drive the gas inward (Kormendy & Kennicutt 2004; Romeo & Fathi 2016). Another possibility could be the triggering of star formation due to positive AGN feedback, with in situ star formation in AGN-driven outflows (Maiolino et al. 2017; Gallagher et al. 2019), and more-luminous AGNs producing more frequent and stronger outflows (Fiore et al. 2017; Rakshit & Woo 2018; Fluetsch et al. 2019; but see Baron & Netzer 2019; Davies et al. 2020; Shangguan et al. 2020a; Molina et al. 2022; Ramos Almeida et al. 2022). The role of gas-rich major mergers cannot be overlooked, as they offer a natural explanation for the triggering of an AGN (e.g., Hopkins et al. 2008), specially for more-luminous active galaxies (Treister et al. 2012). However, not all the galaxies hosting a luminous AGN present evidence of merger activity (e.g., Koss et al. 2011; Kim et al. 2017; Zhao et al. 2019, 2021). The relative fraction of early-type and late-type low-z quasar hosts depends only on stellar mass, and not on bolometric luminosity or Eddington ratio (Zhuang & Ho 2022). We highlight this in Figure 9 where, apart from the mergers likely presenting shorter depletion times, we find no trend between $t_{\rm dep}$ and the AGN properties with galaxy morphology. The only clue that remains is the weak correlation between the Eddington ratio and the host galaxy molecular gas fraction, possibly implying an underlying role of gravitational instabilities or the fast inflow of cold gas in producing nuclear starbursts and the fueling of the BHs.

6. Conclusions

We present new NOEMA observations of the CO(2–1) line for eight of the most-luminous PG quasar host galaxies at $z \lesssim 0.5$. We detect CO(2–1) emission in three objects, doubling the number of most-luminous PG quasar host galaxies with line emission detection. Combined with already published observations for active galaxies, we assemble CO measurements for a broad sample of $z \lesssim 0.5$ type 1 AGNs covering ∼3 decades in AGN luminosity. This sample is used to investigate the relations between AGN properties, molecular gas properties, and star formation efficiency of the host galaxies. The systems with nondetected CO emission are treated as censored data. We summarize our conclusions as follows:

1. The luminous AGNs ($\lambda L_{5100} \gtrsim 10^{45.5}$ erg s^{-1}) observed by NOEMA possesses CO emission consistent with the expectations from the far-IR emission. Overall, the total gas mass predicted from the cold dust emission, and after subtracting the extended atomic gas content, is well matched with the molecular gas mass within an accuracy of ∼0.40 dex, with some small variations depending on the host galaxy morphological type.
2. The PG quasar and CARS AGN host galaxies follow a tight, linear $L_{\rm IR} - L'_{\rm CO}$ correlation consistent with that found for starburst galaxies (Shangguan et al. 2020b). The BASS AGNs follow a similar correlation, but they show a zero-point offset placing them on the relation for normal star-forming galaxies.
3. We find a weak correlation between CO(2–1) line luminosity and AGN luminosity, as well as between molecular gas fraction and Eddington ratio. The former correlation vanishes when considering the cosmic evolution of the gas content in galaxies and that the more-luminous AGN hosts are found at higher redshifts, meaning that the AGN luminosity is not correlated with host galaxy global molecular gas content. The second correlation points to the role of host galaxy gravitational instabilities or the fast inflow of cold gas in triggering AGN activity. Both findings suggest an ineffective role of negative AGN feedback.

We thank the anonymous referee for helpful comments and suggestions. We acknowledge support from the National Science Foundation of China (grant Nos. 11721303, 11991052, 12011540375, and 12233001) and the China Manned Space Project (grant Nos. CMS-CSST-2021-A04 and CMS-CSST-2021-A06). R.W. acknowledges support from the National Science Foundation of China grant No. 12173002. This work was funded by ANID—Millennium Science Initiative Program—ICN12_009 (F.E.B.), CATA-BASAL—FB210003 (F.E.B., E.T.), and FONDECYT Regular—1190818

(E.T., F.E.B.) and 1200495 (F.E.B., E.T.). We thank to Stefano Antonellini for his support during the NOEMA data reduction process. This work is based on observations carried out under project number W21CI with the IRAM NOEMA Interferometer. IRAM is supported by INSU/CNRS (France), MPG (Germany), and IGN (Spain).

Software: ASTROPY (Astropy Collaboration et al. 2013; Price-Whelan et al. 2018), MATPLOTLIB (Hunter 2007), NUMPY (Oliphant 2006), GILDAS (Guilloteau & Lucas 2000).

Appendix
Radio Continuum Measurements

Radio continuum measurements collated from the literature for the eight sources presented in this work (Table 4).

Table 4
Radio Continuum Measurements

Object	Frequency (GHz)	S_ν (mJy)	Reference
(1)	(2)	(3)	(4)
PG 1049−005	1.4	0.82 ± 0.14	Becker et al. (1995)
	5.0	0.48 ± 0.03	Kellermann et al. (1989)
	8.5	0.37 ± 0.07	Baldi et al. (2022)
	45	<0.18*	Baldi et al. (2022)
PG 1100+772	1.4	2341 ± 79	Condon et al. (1998)
	2.7	1415 ± 40	Laing & Peacock (1980)
	5.0	775 ± 30	Laing & Peacock (1980)
	10.7	375 ± 19	Laing & Peacock (1980)
	14.9	310 ± 20	Laing & Peacock (1980)
	31.4	330 ± 130	Geldzahler & Kuhr (1983)
PG 1259+593	1.4	<0.45	Condon et al. (1998)
	5.0	<0.3*	Baldi et al. (2022)
	45	<0.15*	Baldi et al. (2022)
PG 1425+267	0.074	2710 ± 360	Cohen et al. (2007)
	0.151	2260 ± 158	Waldram et al. (1996)
	0.365	572 ± 64	Douglas et al. (1996)
	1.4	108 ± 4	Condon et al. (1998)
	4.85	112 ± 16	Gregory & Condon (1991)
PG 1512+370	0.074	9860 ± 1010	Cohen et al. (2007)
	0.365	3003 ± 49	Douglas et al. (1996)
	1.4	990 ± 31	Condon et al. (1998)
	4.85	361 ± 45	Gregory & Condon (1991)
PG 1704+608	1.49	1258 ± 123	Kuehr et al. (1981)
	4.85	590 ± 30	Gregory & Condon (1991)
	10.7	420 ± 20	Kuehr et al. (1981)
PG 2112+059	1.4	3.0 ± 0.4	Condon et al. (1998)
	1.49	2.93 ± 0.38	Barvainis et al. (1996)
	4.89	0.89 ± 0.09	Barvainis et al. (1996)
	4.9	0.89 ± 0.07	Kellermann et al. (1989)
	8.4	0.52 ± 0.05	Barvainis et al. (2005)
	8.48	0.56 ± 0.07	Barvainis et al. (1996)
	14.9	<0.48	Barvainis et al. (1996)
PG 2251+113	0.074	11,840 ± 1240	Cohen et al. (2007)
	0.365	4387 ± 89	Douglas et al. (1996)
	1.4	1436 ± 43	Condon et al. (1998)
	2.7	700	Wright & Otrupcek (1990)
	4.85	615 ± 85	Gregory & Condon (1991)

Note. (1) Source name. (2) Rest-frame frequency. (3) Flux density. (4) Reference. If available, we provide the 3σ flux density upper limit. (*) Upper-limit values were calculated by using the observation rms as input to Equation (2) and assuming an aperture size equal to three times the observation synthesized beam size ($N_A/N_B = 3$).

ORCID iDs

Juan Molina https://orcid.org/0000-0002-8136-8127
Jinyi Shangguan https://orcid.org/0000-0002-4569-9009
Ran Wang https://orcid.org/0000-0003-4956-5742
Luis C. Ho https://orcid.org/0000-0001-6947-5846
Franz E. Bauer https://orcid.org/0000-0002-8686-8737
Ezequiel Treister https://orcid.org/0000-0001-7568-6412

References

Astropy Collaboration, Robitaille, T. P., Tollerud, E. J., et al. 2013, A&A, 558, A33
Baldi, R. D., Laor, A., Behar, E., et al. 2022, MNRAS, 510, 1043
Baron, D., & Netzer, H. 2019, MNRAS, 482, 3915
Barvainis, R., Lehár, J., Birkinshaw, M., Falcke, H., & Blundell, K. M. 2005, ApJ, 618, 108
Barvainis, R., Lonsdale, C., & Antonucci, R. 1996, AJ, 111, 1431
Becker, R. H., White, R. L., & Helfand, D. J. 1995, ApJ, 450, 559
Bellocchi, E., Pereira-Santaella, M., Colina, L., et al. 2022, A&A, 664, A60
Bernhard, E., Grimmett, L. P., Mullaney, J. R., et al. 2019, MNRAS, 483, L52
Bernhard, E., Mullaney, J. R., Daddi, E., Ciesla, L., & Schreiber, C. 2016, MNRAS, 460, 902
Bertram, T., Eckart, A., Fischer, S., et al. 2007, A&A, 470, 571
Bianchi, S., Guainazzi, M., Matt, G., Fonseca Bonilla, N., & Ponti, G. 2009, A&A, 495, 421
Bischetti, M., Feruglio, C., Piconcelli, E., et al. 2021, A&A, 645, A33
Bolatto, A. D., Wong, T., Utomo, D., et al. 2017, ApJ, 846, 159
Boroson, T. A., & Green, R. F. 1992, ApJS, 80, 109
Bower, R. G., Benson, A. J., Malbon, R., et al. 2006, MNRAS, 370, 645
Bruzual, G., & Charlot, S. 2003, MNRAS, 344, 1000
Cicone, C., Brusa, M., Ramos Almeida, C., et al. 2018, NatAs, 2, 176
Cicone, C., Maiolino, R., Sturm, E., et al. 2014, A&A, 562, A21
Circosta, C., Mainieri, V., Lamperti, I., et al. 2021, A&A, 646, A96
Cohen, A. S., Lane, W. M., Cotton, W. D., et al. 2007, AJ, 134, 1245
Cohen, M., Wheaton, W. A., & Megeath, S. T. 2003, AJ, 126, 1090
Condon, J. J., Cotton, W. D., Greisen, E. W., et al. 1998, AJ, 115, 1693
Croton, D. J., Springel, V., White, S. D. M., et al. 2006, MNRAS, 365, 11
Davies, R., Baron, D., Shimizu, T., et al. 2020, MNRAS, 498, 4150
Douglas, J. N., Bash, F. N., Bozyan, F. A., Torrence, G. W., & Wolfe, C. 1996, AJ, 111, 1945
Downes, D., & Solomon, P. M. 1998, ApJ, 507, 615
Draine, B. T., Dale, D. A., Bendo, G., et al. 2007, ApJ, 663, 866
Draine, B. T., & Li, A. 2007, ApJ, 657, 810
Dubois, Y., Peirani, S., Pichon, C., et al. 2016, MNRAS, 463, 3948
Ellison, S. L., Teimoorinia, H., Rosario, D. J., & Mendel, J. T. 2016, MNRAS, 458, L34
Ellison, S. L., Wong, T., Sánchez, S. F., et al. 2021, MNRAS, 505, L46
Evans, A. S., Solomon, P. M., Tacconi, L. J., Vavilkin, T., & Downes, D. 2006, AJ, 132, 2398
Fabian, A. C. 2012, ARA&A, 50, 455
Ferrarese, L., & Merritt, D. 2000, ApJL, 539, L9
Feruglio, C., Fiore, F., Carniani, S., et al. 2015, A&A, 583, A99
Fiore, F., Feruglio, C., Shankar, F., et al. 2017, A&A, 601, A143
Florez, J., Jogee, S., Sherman, S., et al. 2020, MNRAS, 497, 3273
Fluetsch, A., Maiolino, R., Carniani, S., et al. 2019, MNRAS, 483, 4586
Gallagher, R., Maiolino, R., Belfiore, F., et al. 2019, MNRAS, 485, 3409
Gaspari, M., Tombesi, F., & Cappi, M. 2020, NatAs, 4, 10
Gebhardt, K., Bender, R., Bower, G., et al. 2000, ApJL, 539, L13
Geldzahler, B. J., & Kuhr, H. 1983, AJ, 88, 1126
Genzel, R., Tacconi, L. J., Gracia-Carpio, J., et al. 2010, MNRAS, 407, 2091
Girdhar, A., Harrison, C. M., Mainieri, V., et al. 2022, MNRAS, 512, 1608
Gregory, P. C., & Condon, J. J. 1991, ApJS, 75, 1011
Griffin, M. J., Abergel, A., Abreu, A., et al. 2010, A&A, 518, L3
Grimmett, L. P., Mullaney, J. R., Bernhard, E. P., et al. 2020, MNRAS, 495, 1392
Guilloteau, S., & Lucas, R. 2000, in ASP Conf. Ser. 217: Imaging at Radio through Submillimeter Wavelengths, ed. J. G. Mangum & S. J. E. Radford (San Francisco, CA: ASP), 299
Hainline, L. J., Scoville, N. Z., Yun, M. S., et al. 2004, ApJ, 609, 61
Harrison, C. M., Alexander, D. M., Mullaney, J. R., et al. 2012, ApJL, 760, L15
Harrison, C. M., Johnson, H. L., Swinbank, A. M., et al. 2017, MNRAS, 467, 1965
Ho, L. C., & Kim, M. 2009, ApJS, 184, 398

Ho, L. C., & Kim, M. 2015, ApJ, 809, 123
Högbom, J. A. 1974, A&AS, 15, 417
Hopkins, P. F., Hernquist, L., Cox, T. J., & Kereš, D. 2008, ApJS, 175, 356
Hopkins, P. F., Hernquist, L., Martini, P., et al. 2005, ApJL, 625, L71
Hunter, J. D. 2007, CSE, 9, 90
Husemann, B., Davis, T. A., Jahnke, K., et al. 2017, MNRAS, 470, 1570
Husemann, B., Singha, M., Scharwächter, J., et al. 2022, A&A, 659, A124
Ichikawa, K., Ricci, C., Ueda, Y., et al. 2019, ApJ, 870, 31
Iono, D., Wilson, C. D., Yun, M. S., et al. 2009, ApJ, 695, 1537
Isobe, T., Feigelson, E. D., & Nelson, P. I. 1986, ApJ, 306, 490
Jarrett, T. H., Cohen, M., Masci, F., et al. 2011, ApJ, 735, 112
Jarvis, M. E., Harrison, C. M., Mainieri, V., et al. 2020, MNRAS, 498, 1560
Kakkad, D., Mainieri, V., Brusa, M., et al. 2017, MNRAS, 468, 4205
Kellermann, K. I., Sramek, R., Schmidt, M., Green, R. F., & Shaffer, D. B. 1994, AJ, 108, 1163
Kellermann, K. I., Sramek, R., Schmidt, M., Shaffer, D. B., & Green, R. 1989, AJ, 98, 1195
Kennicutt, R. C. 1998, ARA&A, 36, 189
Kim, M., & Ho, L. C. 2019, ApJ, 876, 35
Kim, M., Ho, L. C., Peng, C. Y., et al. 2008, ApJ, 687, 767
Kim, M., Ho, L. C., Peng, C. Y., Barth, A. J., & Im, M. 2017, ApJS, 232, 21
Kirkpatrick, A., Sharon, C., Keller, E., & Pope, A. 2019, ApJ, 879, 41
Kirkpatrick, A., Urry, C. M., Brewster, J., et al. 2020, ApJ, 900, 5
Kormendy, J., & Ho, L. C. 2013, ARA&A, 51, 511
Kormendy, J., & Kennicutt, R. C. 2004, ARA&A, 42, 603
Koss, M., Mushotzky, R., Veilleux, S., et al. 2011, ApJ, 739, 57
Koss, M. J., Strittmatter, B., Lamperti, I., et al. 2021, ApJS, 252, 29
Koss, M. J., Trakhtenbrot, B., Ricci, C., et al. 2022, ApJS, 261, 1
Kroupa, P. 2001, MNRAS, 322, 231
Kuehr, H., Witzel, A., Pauliny-Toth, I. I. K., & Nauber, U. 1981, A&AS, 45, 367
Laing, R. A., & Peacock, J. A. 1980, MNRAS, 190, 903
Lamperti, I., Saintonge, A., Koss, M., et al. 2020, ApJ, 889, 103
Leroy, A. K., Bolatto, A., Gordon, K., et al. 2011, ApJ, 737, 12
Lutz, D., Shimizu, T., Davies, R. I., et al. 2018, A&A, 609, A9
Magorrian, J., Tremaine, S., Richstone, D., et al. 1998, AJ, 115, 2285
Maiolino, R., Russell, H. R., Fabian, A. C., et al. 2017, Natur, 544, 202
Mejía-Restrepo, J. E., Trakhtenbrot, B., Koss, M. J., et al. 2022, ApJS, 261, 5
Michiyama, T., Saito, T., Tadaki, K.-I., et al. 2021, ApJS, 257, 28
Molina, J., Ho, L. C., Wang, R., et al. 2022, ApJ, 935, 72
Molina, J., Ho, L. C., Wang, R., et al. 2023, ApJ, 944, 30
Molina, J., Wang, R., Shangguan, J., et al. 2021, ApJ, 908, 231
Morganti, R. 2017, NatAs, 1, 596
Mushotzky, R. F., Shimizu, T. T., Meléndez, M., & Koss, M. 2014, ApJL, 781, L34
Nelson, D., Pillepich, A., Springel, V., et al. 2018, MNRAS, 475, 624
Nenkova, M., Sirocky, M. M., Ivezić, Ž., & Elitzur, M. 2008a, ApJ, 685, 147
Nenkova, M., Sirocky, M. M., Nikutta, R., Ivezić, Ž., & Elitzur, M. 2008b, ApJ, 685, 160
Oliphant, T. E. 2006, A Guide to NumPy, Vol. 1 (USA: Trelgol Publishing) https://web.mit.edu/dvp/Public/numpybook.pdf
Perna, M., Brusa, M., Cresci, G., et al. 2015, A&A, 574, A82
Perna, M., Sargent, M. T., Brusa, M., et al. 2018, A&A, 619, A90
Petric, A. O., Ho, L. C., Flagey, N. J. M., & Scoville, N. Z. 2015, ApJS, 219, 22
Pitchford, L. K., Hatziminaoglou, E., Feltre, A., et al. 2016, MNRAS, 462, 4067
Planck Collaboration, Ade, P. A. R., Aghanim, N., et al. 2016, A&A, 594, A13
Poglitsch, A., Waelkens, C., Geis, N., et al. 2010, A&A, 518, L2
Price-Whelan, A. M., Sipőcz, B. M., Günther, H. M., et al. 2018, AJ, 156, 123
Privon, G. C., Ricci, C., Aalto, S., et al. 2020, ApJ, 893, 149
Rakshit, S., & Woo, J.-H. 2018, ApJ, 865, 5
Ramos Almeida, C., Bischetti, M., García-Burillo, S., et al. 2022, A&A, 658, A155
Reeves, J. N., & Turner, M. J. L. 2000, MNRAS, 316, 234
Richards, G. T., Lacy, M., Storrie-Lombardi, L. J., et al. 2006, ApJS, 166, 470
Romeo, A. B., & Fathi, K. 2016, MNRAS, 460, 2360
Rosario, D. J., Burtscher, L., Davies, R. I., et al. 2018, MNRAS, 473, 5658
Rosario, D. J., Santini, P., Lutz, D., et al. 2012, A&A, 545, A45
Rosario, D. J., Santini, P., Lutz, D., et al. 2013, ApJ, 771, 63
Salvestrini, F., Gruppioni, C., Hatziminaoglou, E., et al. 2022, A&A, 663, A28
Sanders, D. B., Soifer, B. T., Elias, J. H., et al. 1988, ApJ, 325, 74
Sandstrom, K. M., Leroy, A. K., Walter, F., et al. 2013, ApJ, 777, 5
Savage, R. S., & Oliver, S. 2007, ApJ, 661, 1339
Schaye, J., Crain, R. A., Bower, R. G., et al. 2015, MNRAS, 446, 521
Scholtz, J., Alexander, D. M., Harrison, C. M., et al. 2018, MNRAS, 475, 1288
Schulze, A., Silverman, J. D., Daddi, E., et al. 2019, MNRAS, 488, 1180
Scoville, N. Z., Frayer, D. T., Schinnerer, E., & Christopher, M. 2003, ApJL, 585, L105
Shangguan, J., Ho, L. C., Bauer, F. E., Wang, R., & Treister, E. 2020a, ApJ, 899, 112
Shangguan, J., Ho, L. C., Bauer, F. E., Wang, R., & Treister, E. 2020b, ApJS, 247, 15
Shangguan, J., Ho, L. C., & Xie, Y. 2018, ApJ, 854, 158
Shi, Y., Rieke, G. H., Ogle, P. M., Su, K. Y. L., & Balog, Z. 2014, ApJS, 214, 23
Shimizu, T. T., Meléndez, M., Mushotzky, R. F., et al. 2016, MNRAS, 456, 3335
Shimizu, T. T., Mushotzky, R. F., Meléndez, M., et al. 2017, MNRAS, 466, 3161
Sijacki, D., Vogelsberger, M., Genel, S., et al. 2015, MNRAS, 452, 575
Silpa, S., Kharb, P., Ho, L. C., et al. 2020, MNRAS, 499, 5826
Skrutskie, M. F., Cutri, R. M., Stiening, R., et al. 2006, AJ, 131, 1163
Smirnova-Pinchukova, I., Husemann, B., Davis, T. A., et al. 2022, A&A, 659, A125
Solomon, P. M., & Vanden Bout, P. A. 2005, ARA&A, 43, 677
Somerville, R. S., Hopkins, P. F., Cox, T. J., Robertson, B. E., & Hernquist, L. 2008, MNRAS, 391, 481
Stanley, F., Alexander, D. M., Harrison, C. M., et al. 2017, MNRAS, 472, 2221
Stemo, A., Comerford, J. M., Barrows, R. S., et al. 2020, ApJ, 888, 78
Tacconi, L. J., Genzel, R., Saintonge, A., et al. 2018, ApJ, 853, 179
Torbaniuk, O., Paolillo, M., Carrera, F., et al. 2021, MNRAS, 506, 2619
Treister, E., Schawinski, K., Urry, C. M., & Simmons, B. D. 2012, ApJL, 758, L39
Veilleux, S., Maiolino, R., Bolatto, A. D., & Aalto, S. 2020, A&ARv, 28, 2
Vestergaard, M., & Peterson, B. M. 2006, ApJ, 641, 689
Vietri, G., Garilli, B., Polletta, M., et al. 2022, A&A, 659, A129
Vito, F., Maiolino, R., Santini, P., et al. 2014, MNRAS, 441, 1059
Waldram, E. M., Yates, J. A., Riley, J. M., & Warner, P. J. 1996, MNRAS, 282, 779
Ward, S. R., Harrison, C. M., Costa, T., & Mainieri, V. 2022, MNRAS, 514, 2936
Woo, J.-H., Son, D., & Rakshit, S. 2020, ApJ, 901, 66
Wright, A., & Otrupcek, R. 1990, PKS, 1990
Wright, E. L., Eisenhardt, P. R. M., Mainzer, A. K., et al. 2010, AJ, 140, 1868
Xie, Y., & Ho, L. C. 2022, ApJ, 925, 218
Xie, Y., Ho, L. C., Zhuang, M.-Y., & Shangguan, J. 2021, ApJ, 910, 124
Yesuf, H. M., & Ho, L. C. 2020, ApJ, 901, 42
Young, J. E., Eracleous, M., Shemmer, O., et al. 2014, MNRAS, 438, 217
Zhang, Z., Shi, Y., Rieke, G. H., et al. 2016, ApJL, 819, L27
Zhao, D., Ho, L. C., Zhao, Y., Shangguan, J., & Kim, M. 2019, ApJ, 877, 52
Zhao, Y., Ho, L. C., Shangguan, J., et al. 2021, ApJ, 911, 94
Zhuang, M.-Y., & Ho, L. C. 2020, ApJ, 896, 108
Zhuang, M.-Y., & Ho, L. C. 2022, ApJ, 934, 130
Zhuang, M.-Y., Ho, L. C., & Shangguan, J. 2018, ApJ, 862, 118
Zhuang, M.-Y., Ho, L. C., & Shangguan, J. 2021, ApJ, 906, 38